Research article

Anoop Thomas, Anjali Jayachandran, Lucas Lethuillier-Karl, Robrecht M.A. Vergauwe, Kalaivanan Nagarajan, Eloise Devaux, Cyriaque Genet, Joseph Moran and Thomas W. Ebbesen*

Ground state chemistry under vibrational strong coupling: dependence of thermodynamic parameters on the Rabi splitting energy

https://doi.org/10.1515/nanoph-2019-0340
Received September 2, 2019; revised October 16, 2019; accepted October 27, 2019

Abstract: Vibrational strong coupling (VSC) is currently emerging as a tool to control chemical dynamics. Here we study the impact of strong coupling strength, given by the Rabi splitting energy ($\hbar\Omega_R$), on the thermodynamic parameters associated with the transition state of the desilylation reaction of the model molecule 1-phenyl-2-trimethylsilylacetylene. Under VSC, the enthalpy and entropy of activation determined from the temperature-dependent kinetic studies varied nonlinearly with the coupling strength. The thermodynamic parameters of the noncavity reaction did not show noticeable variation, ruling out concentration effects other than the enhanced $\hbar\Omega_R$ for the changes observed under VSC. The difference between the total free energy change under VSC and in noncavity was relatively smaller possibly because the enthalpy and entropy of activation compensate each other. This thermodynamic study gives more insight into the role of collective strong coupling on the transition state that leads to modified dynamics and branching ratios.

Keywords: vibrational strong coupling; vibrations; chemical dynamics; thermodynamics; transition states; microcavities.

***Corresponding author: Thomas W. Ebbesen,** University of Strasbourg, CNRS, ISIS and icFRC, 8 allée G. Monge, 67000 Strasbourg, France, e-mail: ebbesen@unistra.fr
Anoop Thomas, Anjali Jayachandran, Lucas Lethuillier-Karl, Robrecht M.A. Vergauwe, Kalaivanan Nagarajan, Eloise Devaux, Cyriaque Genet and Joseph Moran: University of Strasbourg, CNRS, ISIS and icFRC, 8 allée G. Monge, 67000 Strasbourg, France.
https://orcid.org/0000-0001-8702-4934 (A. Thomas)

1 Introduction

Light–matter strong coupling is evolving as a physical tool for chemists to control chemical reactivity [1–10]. This was triggered by the modified spiropyran–merocyanine photoisomerisation dynamics under the electronic strong coupling (ESC) [2] and further fuelled by the development of vibrational strong coupling (VSC), where the vibrational mode of a molecule is strongly coupled [11–18]. Vibrational strong coupling was envisioned to alter the rates and yields of ground state chemical reactions as the latter involves the scission and formation of chemical bonds and therefore vibrations [11]. The retarded kinetics of the desilylation of 1-phenyl-2-trimethylsilylacetylene (PTA) provided the first evidence for a VSC-controlled chemical reaction [3]. Subsequent experiments under VSC showed that the reactions can be accelerated [7, 8], and the chemical landscape could be modified in such a way that the product branching ratio is altered [6]. Remarkably, the reactivity can also be controlled by the strong coupling of solvent vibrational modes [8, 9]. Various theoretical models have been developed recently, which support the modified chemical dynamics under strong coupling [19–26]. However, the mechanistic details of chemical reactions under VSC are not well understood, although a clear change in the activation barrier is observed in experimental [3, 6–8] and in theoretical studies [24–26]. The present study aims to provide further insights into the transition state (TS) changes under VSC by monitoring the thermodynamic parameters of the desilylation reaction of PTA as a function of the strong coupling strength.

Light–matter strong coupling, for example VSC, occurs when the resonance energy exchange between the molecular vibration and the eigen mode of an electromagnetic cavity (Fabry–Pérot cavity) proceeds faster than any other decay process [1]. This results in hybrid light–matter states, called the polaritonic states (P+ and P–), which are

visible as split vibrational modes separated by the Rabi splitting energy ($\hbar\Omega_R$) in the absorption spectrum of the molecule. The formation of polaritonic states is schematically shown in Figure 1A. The coupling strength, $\hbar\Omega_R$, is often decisive in the modification of molecular properties, and its magnitude for a molecule can be calculated with the Jaynes–Cummings two-state model, which reduces to (1) in the absence of any dissipation:

$$\hbar\Omega_R = 2d\sqrt{\frac{\hbar\omega}{2\varepsilon_0 v}} \times \sqrt{n_{ph}+1} \quad (1)$$

where d is the transition dipole moment of the molecule (which is determined by the derivative of the permanent dipole moment of the vibrational mode), $\hbar\omega$ is the optical resonance, ε_0 is the vacuum permittivity, v is the volume of the electromagnetic mode, and n_{ph} gives the number photons involved in the strong coupling. Detailed description of strong light–matter coupling, and its impact on molecular and material properties can be found in [1, 27–33]. For discussions specific to the physics of VSC, the reader is referred to [11] and [16]. The last part of (1) points out that $\hbar\Omega_R$ has a residual value known as vacuum Rabi splitting energy even in the absence of real photons. In other words, the zero-point energy fluctuations of the cavity enable the formation of light–matter hybrid states in the dark. The experiments reported here are carried out under this regime, such that the weak IR light used to intermittently probe the system does not increase the $\hbar\Omega_R$ in this collective coupling condition. The magnitude of $\hbar\Omega_R$ is varied only when the number of molecules (N) involved in the coupling process is changed. This is because the volume of a single electromagnetic mode can accommodate a large number of molecules. The wave functions of the hybrid states are delocalised over all the molecules interacting with the cavity mode, and therefore the $\hbar\Omega_R \propto \sqrt{N/v} = \sqrt{C}$, where C is the concentration of the molecule. This scenario is schematically shown in Figure 1A with VSC of PTA as an example.

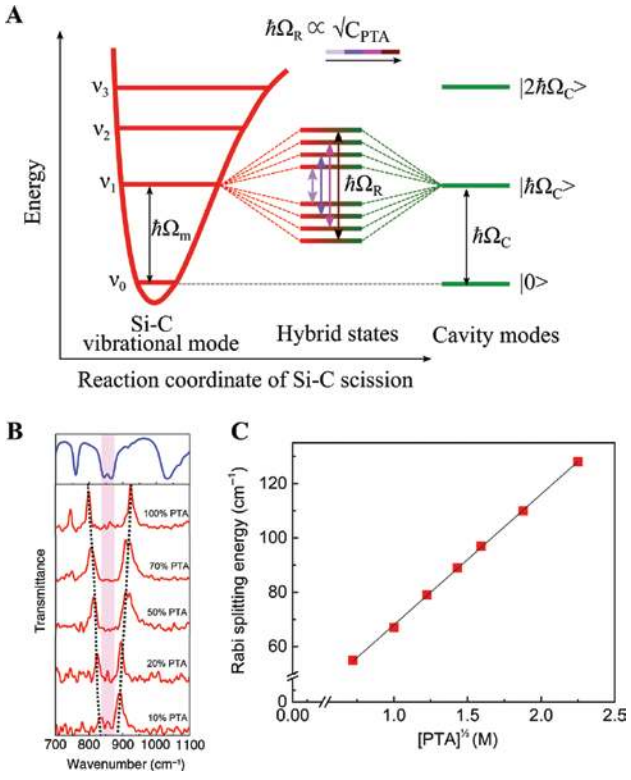

Figure 1: Formation of polaritonic states and VSC of Si–C stretching modes of PTA.
(A) Schematic illustration of the formation of polaritonic states P+ and P– and the modulation of Rabi splitting energy as the concentration of PTA (C_{PTA}) is varied. (B) FT-IR transmission spectra showing the vibrational modes of PTA in methanol (blue curve) and the Rabi splitting corresponding to the VSC of the Si–C stretching modes as a function of C_{PTA}. The shaded region shows the width of the Si–C stretching vibration, and the dotted lines are guide to the eyes. (C) The plot showing the linear dependence of Rabi splitting energy on the square root of C_{PTA}.

2 Results and discussion

The desilylation of PTA (Supplementary Material, Figure S1) was chosen as the model reaction for the present study. The VSC of the Si–C stretching vibrational mode (ν_{Si-C}; 860 cm^{-1}, blue curve in Figure 1B) of PTA has shown to retard the Si–C bond scission dynamics [3], prompting us to do a detailed thermodynamic study, varying the $\hbar\Omega_R$. Vibrational strong coupling of the ν_{Si-C} of PTA is achieved using a Fabry–Pérot cavity assembled in a temperature-controllable and demountable IR cell (purchased from Specac) equipped with holes to inject the liquids. An air-filled Fabry–Pérot cavity (empty cavity) is built in the IR cell by placing a Mylar spacer (6 ± 1 μm thick with a hollow central region) on top of an Au-coated ZnSe window (bottom mirror), which is then covered by a top mirror of Au sputtered on a ZnSe substrate having an inlet and outlet hole for sample injection. To protect the Au from the reactants, a 200-nm-thick SiO_2 (glass) was deposited on top of the Au mirrors. The IR cell is then closed by tightening the screws on the top lid. Such an empty cavity has many equally spaced modes in the IR whose periodicity is determined by the path length of the cavity (Figure S2). Using a screwdriver, the empty cavity path length is then fine-tuned by adjusting the screws on the cell such that

upon injection of the reaction mixture one of the modes of the cavity will be at 860 cm^{-1}. In other words, during the reaction under VSC, the cavity mode will be on resonance with the ν_{Si-C} of PTA at normal incidence. For more details on cavity preparation, see Supplementary Materials and earlier reports [6, 13].

The VSC of the ν_{Si-C} as a function of the concentration of PTA (C_{PTA}) was analysed first to determine a lower limit for VSC in the experiments. Different solutions of varying C_{PTA} (5–0.5 M) were prepared by the addition of methanol to a neat PTA and were then injected to a tuned cavity described earlier. The VSC of the ν_{Si-C} of PTA in each experiment was evident from appearance of the split peaks (P+ and P–) in the IR transmission spectra shown in Figure 1B (red curves). The $\hbar\Omega_R$ of the strongly coupled ν_{Si-C} reduced from 128 cm^{-1} to 55 cm^{-1} with decreasing C_{PTA}. The lowest C_{PTA} used (0.5 M; 10% by volume in methanol) also satisfies the strong coupling conditions as its Rabi splitting energy (55 cm^{-1}) is larger than the full width at half maximum of the cavity mode (28 cm^{-1}) and the width of the ν_{Si-C} (39 cm^{-1}). Further dilution of PTA with methanol resulted in reduced signal and was difficult to distinguish in the noisy background. The variation of $\hbar\Omega_R$ scaled linearly with square root of the C_{PTA}, as shown in Figure 1C, confirming strong coupling for all the concentrations studied.

To analyse the impact of $\hbar\Omega_R$ on the thermodynamic parameters of the desilylation under VSC, the C_{PTA} in the reaction mixture [a freshly prepared homogeneous solution of PTA and tetrabutyl ammonium fluoride (TBAF) in methanol] was varied from 0.5 to 2.5 M in steps of 0.5 M, while maintaining the fixed concentration of TABF (0.5 M). The presence of TBAF facilitates the desilylation reaction at room temperature [34]. A higher C_{PTA} resulted in immiscible solutions when mixed with TBAF and methanol and is therefore not suitable for experiments under VSC. The TBAF concentration was fixed based on the half-life of the reaction outside the cavity for the lowest C_{PTA} and the homogeneity of the reaction mixtures for all the C_{PTA} used.

In order to extract the thermodynamic parameters of the desilylation of PTA under VSC, the rate constants for the reaction with a fixed $\hbar\Omega_R$ (C_{PTA}) in a small range of temperature (20°C–40°C) were determined as follows. The IR cell containing the tuned empty cavity is placed in a temperature-controlled jacket and is allowed to equilibrate to the set temperature. Subsequently, the reaction mixture is injected to the cavity without removing it from the temperature-controlled jacket. Precise tuning of the cavity mode to the ν_{Si-C} of PTA is ensured in every experiment and confirmed by the appearance of the P+ and P– in the IR transmission spectra. The rate constant of the silyl bond scission was determined following the relative shift of a higher-order cavity mode as explained in the earlier reports [3, 6] and in the Supplementary Material (Figure S3). For comparison, reactions were also carried out outside the cavity (noncavity), as exactly described for experiments under VSC, using a cell made of SiO_2-coated ZnSe. Plots showing the comparison of desilylation kinetics at 25°C, under VSC and noncavity, are given in the Supplementary Material (Figure S4).

The temperature-dependent rate constants of the desilylation for reaction mixtures with different $\hbar\Omega_R$ were then analysed based on the TS Eyring equation:

$$k = \frac{k_B T}{h} \exp\left(-\frac{\Delta H^{\ddagger}}{RT} + \frac{\Delta S^{\ddagger}}{R} \right) \quad (2)$$

where k is the rate constant, k_B is the Boltzmann constant, T is the temperature, h is Plank's constant, and R is the universal gas constant. From the slope and the intercept of the Eyring plot, a plot of rate constant against inverse of temperature, enthalpy ($\Delta H^{\ddagger}$), and entropy ($\Delta S^{\ddagger}$) of activation of the TS is determined. The Eyring plots for various values of $\hbar\Omega_R$ and its comparison for a noncavity reaction for the same C_{PTA} are shown in Figure 2. A clear change in slope of the Eyring plot is visible for reactions under VSC with respect to the variation in the $\hbar\Omega_R$, whereas those for the noncavity experiments remained more or less the same for the different C_{PTA}. The plots were then analysed quantitatively to determine the values of $\Delta H^{\ddagger}$, $\Delta S^{\ddagger}$, and the corresponding free energy of the TS ($\Delta G^{\ddagger}$).

The red squares in Figure 3A and B show the variation of the $\Delta H^{\ddagger}$ and $T\Delta S^{\ddagger}$ values under VSC as a function of $\hbar\Omega_R$. As clearly seen in Figure 3A, $\Delta H^{\ddagger}$ (35 ± 4 kJ mol^{-1}, lowest $\hbar\Omega_R$) more than doubled to 84 ± 8 kJ mol^{-1} for the reaction proceeding under the largest $\hbar\Omega_R$, indicating a higher enthalpy requirement for the desilylation reaction with increasing coupling strength. The noncavity experiments did not exhibit noticeable variation in $\Delta H^{\ddagger}$ as a function of C_{PTA} (Figure 3A, blue circles), revealing that the change under VSC is not a concentration effect. The $T\Delta S^{\ddagger}$ (-49 ± 6 kJ mol^{-1} for the lowest $\hbar\Omega_R$, $T = 298$ K) underwent a decrease in magnitude and nearly changed its sign to -1 ± 7 kJ mol^{-1} for the largest $\hbar\Omega_R$ studied here, representing a gradual change from an organised to a less-ordered TS as the strong coupling strength is increased. Again, it can be seen that in the case of the noncavity conditions no such change in the $T\Delta S^{\ddagger}$ is observed (Figure 3B, blue circles). Figure 3C shows $\Delta(\Delta G^{\ddagger})$, the difference between $\Delta G^{\ddagger}$ of the reaction under VSC and noncavity, as a function of $\hbar\Omega_R$. The variation in $\Delta(\Delta G^{\ddagger})$ is relatively small compared to the large changes observed for $\Delta H^{\ddagger}$ and $\Delta S^{\ddagger}$, because the latter

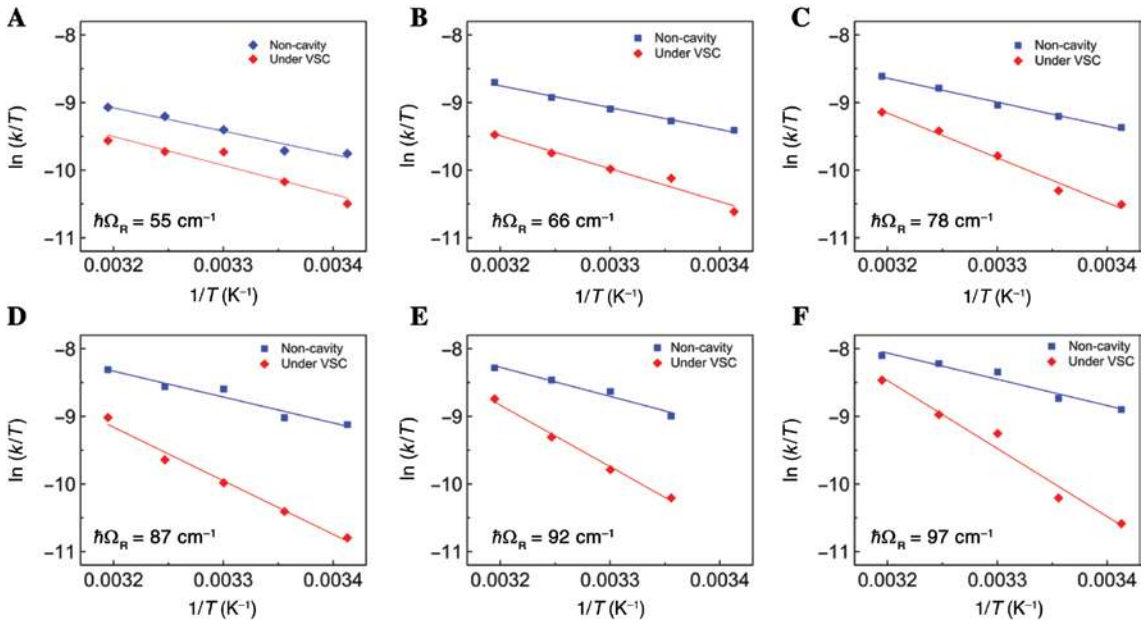

Figure 2: Eyring plots of reaction under VSC and noncavity conditions.
(A–F) Plots of reaction rate as a function of temperature under VSC (red diamonds) for the various Rabi splitting energies and the corresponding plot for noncavity reactions (blue squares). The different values of $\hbar\Omega_R$ are shown in the plots. Least-squares method was used to fit the data, and the goodness of the fit was assessed based on the coefficient of determination (R^2) value. For each fit, R^2 value was ≥0.95.

compensate each other. The upward trend of $\Delta(\Delta G^{\ddagger})$ with the increase of $\hbar\Omega_R$ is representative of the higher energy requirement for the desilylation under VSC compared to the noncavity and leads to the retarded reactivity up to a factor 4.5 as shown in Figure 3D and as reported earlier [3].

It is remarkable that although the changes in the thermodynamic parameters follow the Rabi splitting, their magnitude is much greater than the VSC induced $\hbar\Omega_R$. This indicates that the effect of VSC is not only an energetic one on the potential energy surface leading to the products, it must also imply a change in reaction mechanism, which is confirmed by the evolution of $\Delta H^{\ddagger}$ and $\Delta S^{\ddagger}$ as discussed elsewhere [3]. It is interesting to see that the VSC has a retarding effect on the reaction, which could be understood by looking into the formation and organisation of the TS of the rate-limiting step.

The thermodynamic parameter $\Delta H^{\ddagger}$ mostly represents the reorganisation energy requirement for the formation of the TS, and $\Delta S^{\ddagger}$ primarily indicates the degree of organisation of the TS [35]. Under ambient conditions, the reaction studied here proceeds through a pentacoordinate intermediate and follows an associative mechanism with an ordered TS [35–37]. The lower value of $\Delta H^{\ddagger}$ (30 ± 4 kJ mol^{-1}) and the large negative value of $T\Delta S^{\ddagger}$ (-54 ± 6 kJ mol^{-1}, $T = 298$ K) for the noncavity experiments agree well with the associative mechanism and with a TS that is more reactant/intermediate-like as schematically displayed in Figure 4A. Interestingly, the thermodynamic data show that the reaction proceeds through a more product-like TS as shown in Figure 4B under VSC. The dissociative TS requires higher energy as it is more bond-breaking, and it is less strained because of the tetrahedral-like structure. This could mean that the intermediate generated under VSC is easier to form but more stable than the noncavity case either by a charge stabilisation or by anisotropic interactions induced by light–matter coupling. For example, mode selective chemistry experiments have shown that TS control of the reaction can be modulated by anisotropic forces either to enhance or suppress a particular reaction path [38]. In other words, the role of strong coupling could be more important in determining the position and structure of the TS as shown in recent experimental [6, 8] and theoretical studies [23, 24].

In summary, we have shown that the thermodynamic parameters of a chemical reaction under VSC are indeed dependent on the strong coupling strength. This further illustrates that the polaritonic states are delocalised over all the molecules involved in the strong coupling and act collectively, even though the reactions are ultimately localised on single molecules. The observed changes in chemical dynamics of the present system, despite the relatively weak Rabi splitting energy compared to the TS energy of

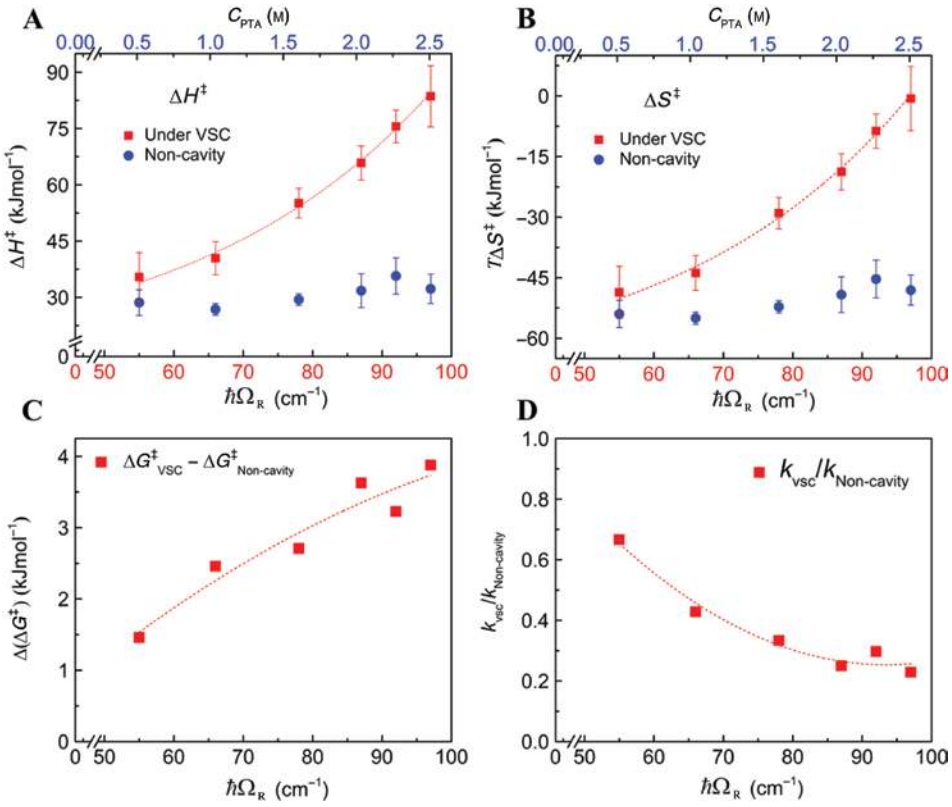

Figure 3: Variation of thermodynamic parameters of as a function of Rabi splitting energy.
Plots showing the changes in (A) the enthalpy of activation and (B) entropy of activation ($T\Delta S^{\ddagger}$, $T = 298$ K) under VSC (red squares). The blue circles represent the corresponding noncavity values for the various C_{PTA} shown in top axis. (C) Shows the difference between the free energy of activation under VSC with increasing $\hbar\Omega_R$ at normal incidence and the noncavity situation at the same C_{PTA}. (D) The decrease in the ratio of the reaction rates at 25°C under VSC for various values of $\hbar\Omega_R$ relative to the noncavity situation. The dashed lines are guides to the eye.

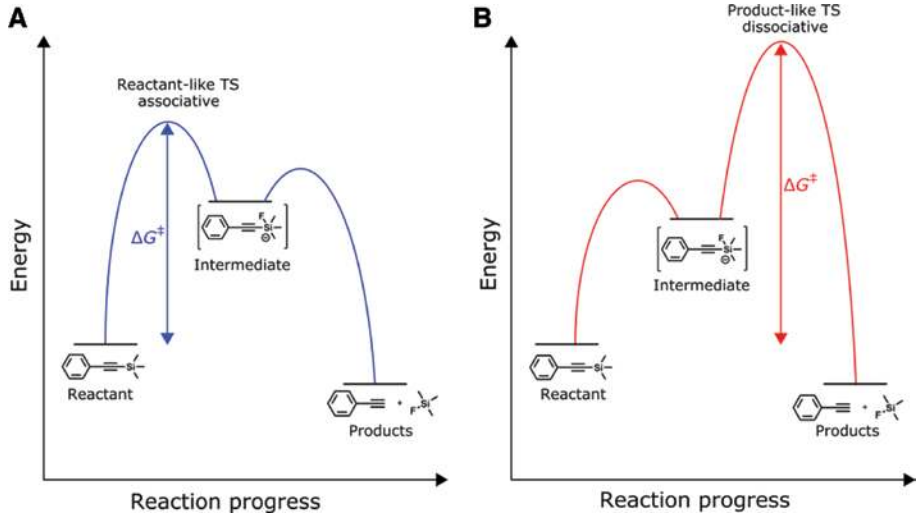

Figure 4: Vibrational strong coupling modifies the reactive landscape to a dissociative path.
Schematic illustration of possible transition states under (A) noncavity and (B) VSC.

the reaction, point to structural changes in the TS under VSC. With more experiments and theoretical understanding about the TS changes under strong coupling, it should be possible to predict the catalytic activity and the product selectivity of reactions controlled by light–matter hybrid states.

Acknowledgements: The authors acknowledge support of the International Center for Frontier Research in Chemistry (icFRC, Strasbourg), the ANR Equipex Union (ANR-10-EQPX-52-01, Funder Id: http://dx.doi.org/10.13039/501100001665), the Labex NIE projects (ANR-11-LABX-0058 NIE, Funder Id: http://dx.doi.org/10.13039/501100001665), and CSC (ANR-10-LABX- 0026 CSC, Funder Id: http://dx.doi.org/10.13039/501100001665) within the Investissement d'Avenir program ANR-10-IDEX-0002-02, Funder Id: http://dx.doi.org/10.13039/501100001665, the ERC (project no. 788482 MOLUSC and no. 639170 CARBONFIX), and QuantERA projet RouTe.

References

[1] Ebbesen TW. Hybrid light–matter states in a molecular and material science perspective. Acc Chem Res 2016;49:2403–12.
[2] Hutchison JA, Schwartz T, Genet C, Devaux E, Ebbesen TW. Modifying chemical landscapes by coupling to vacuum fields. Angew Chem Int Ed 2012;51:1592–6.
[3] Thomas A, George J, Shalabney A, et al. Ground-state chemical reactivity under vibrational coupling to the vacuum electromagnetic field. Angew Chem Int Ed 2016;55:11462–6.
[4] Munkhbat B, Wersäll M, Baranov DG, Antosiewicz TJ, Shegai T. Suppression of photo-oxidation of organic chromophores by strong coupling to plasmonic nanoantennas. Sci Adv 2018;4:eaas9552.
[5] Peters VN, Faruk MO, Asane J, et al. Effect of strong coupling on photodegradation of the semiconducting polymer P3HT. Optica 2019;6:318–25.
[6] Thomas A, Lethuillier-Karl L, Nagarajan K, et al. Tilting a ground-state reactivity landscape by vibrational strong coupling. Science 2019;363:615–9.
[7] Hiura H, Shalabney A, George J. Vacuum-field catalysis: accelerated reactions by vibrational ultra strong coupling. ChemRxiv 2018. doi:10.26434/chemrxiv.7234721.v4.
[8] Lather J, Bhatt P, Thomas A, Ebbesen TW, George J. Cavity catalysis by cooperative vibrational strong coupling of reactant and solvent molecules. Angew Chem Int Ed 2019;58:10635–8.
[9] Vergauwe RMA, Thomas A, Nagarajan K, et al. Modification of enzyme activity by vibrational strong coupling of water. Angew Chem Int Ed 2019;58:15324–8.
[10] Stranius K, Hertzog M, Börjesson K. Selective manipulation of electronically excited states through strong light–matter interactions. Nat Commun 2018;9:2273.
[11] Shalabney A, George J, Hutchison J, Pupillo G, Genet C, Ebbesen TW. Coherent coupling of molecular resonators with a microcavity mode. Nat Commun 2015;6:5981.
[12] Long JP, Simpkins BS. Coherent coupling between a molecular vibration and Fabry–Perot optical cavity to give hybridized states in the strong coupling limit. ACS Photonics 2015;2:130–6.
[13] George J, Shalabney A, Hutchison JA, Genet C, Ebbesen TW. Liquid-phase vibrational strong coupling. J Phys Chem Lett 2015;6:1027–31.
[14] Casey SR, Sparks JR. Vibrational strong coupling of organometallic complexes. J Phys Chem C 2016;120:28138–43.
[15] Vergauwe RMA, George J, Chervy T, et al. Quantum strong coupling with protein vibrational modes. J Phys Chem Lett 2016;7:4159–64.
[16] George J, Chervy T, Shalabney A, et al. Multiple Rabi splittings under ultrastrong vibrational coupling. Phys Rev Lett 2016;117:153601.
[17] Damari R, Weinberg O, Krotkov D, et al. Strong coupling of collective intermolecular vibrations in organic materials at terahertz frequencies. Nat Commun 2019;10:1–8.
[18] Muallem M, Palatnik A, Nessim GD, Tischler YR. Strong light–matter coupling and hybridization of molecular vibrations in a low-loss infrared microcavity. J Phys Chem Lett 2016;7:2002–8.
[19] Herrera F, Spano FC. Cavity-controlled chemistry in molecular ensembles. Phys Rev Lett 2016;116:238301.
[20] Galego J, Garcia-Vidal FJ, Feist J. Suppressing photochemical reactions with quantized light fields. Nat Commun 2016;7:13841.
[21] Du M, Ribeiro RF, Yuen-Zhou J. Remote control of chemistry in optical cavities. Chem 2019;5:1167–81.
[22] Groenhof G, Toppari JJ. Coherent light harvesting through strong coupling to confined light. J Phys Chem Lett 2018;9:4848–51.
[23] Schäfer C, Ruggenthaler M, Appel H, Rubio A. Modification of excitation and charge transfer in cavity quantum-electrodynamical chemistry. PNAS 2019;116:4883–92.
[24] Climent C, Galego J, Garcia-Vidal FJ, Feist J. Plasmonic nanocavities enable self-induced electrostatic catalysis. Angew Chem Int Ed 2019;58:8698–702.
[25] Campos-Gonzalez-Angulo J, Ribeiro RF, Yuen-Zhou J. Resonant catalysis of thermally-activated chemical reactions via vibrational polaritons. Nat Commun 2019;10:article no. 4685.
[26] Flick J, Narang P. Excited-state nanophotonic and polaritonic chemistry with ab initio potential-energy surfaces. arXiv:1907.04646v1 [Physics, Physics:Quant-Ph] 2019.
[27] Törmä P, Barnes WL. Strong coupling between surface plasmon polaritons and emitters: a review. Rep Prog Phys 2014;78:013901.
[28] Ribeiro RF, Martínez-Martínez LA, Du M, Campos-Gonzalez-Angulo J, Yuen-Zhou J. Polariton chemistry: controlling molecular dynamics with optical cavities. Chem Sci 2018;9:6325–39.
[29] Flick J, Rivera N, Narang P. Strong light–matter coupling in quantum chemistry and quantum photonics. Nanophotonics 2018;7:1479–501.
[30] Ruggenthaler M, Tancogne-Dejean N, Flick J, Appel H, Rubio A. From a quantum-electrodynamical light–matter description to novel spectroscopies. Nat Rev Chem 2018;2:0118.
[31] Dovzhenko DS, Ryabchuk SV, Rakovich YP, Nabiev IR. Light–matter interaction in the strong coupling regime: configurations, conditions, and applications. Nanoscale 2018;10:3589–605.

[32] Feist J, Galego J, Garcia-Vidal FJ. Polaritonic chemistry with organic molecules. ACS Photonics 2018;5:205–16.
[33] Hertzog M, Wang M, Mony J, Börjesson K. Strong light–matter interactions: a new direction within chemistry. Chem Soc Rev 2019;48:937–61.
[34] DiLauro AM, Seo W, Phillips ST. Use of catalytic fluoride under neutral conditions for cleaving silicon–oxygen bonds. J Org Chem 2011;76:7352–8.
[35] Carey FA, Sundberg RJ. Advanced organic chemistry: Part A: structure and mechanisms. 5th ed. New York, NY, USA, Springer US, 2007.
[36] Clayden J, Greeves N, Warren SG. Organic chemistry. New York, USA, Oxford University Press Inc., 2012.
[37] Bassindale AR, Taylor PG. Reaction mechanisms of nucleophilic attack at silicon. In: Organic Silicon Compounds (1989). Wiley-Blackwell, 2004:839–92.
[38] Guo H, Liu K. Control of chemical reactivity by transition-state and beyond. Chem Sci 2016;7:3992–4003.

Supplementary Material: The online version of this article offers supplementary material (https://doi.org/10.1515/nanoph-2019-0340).